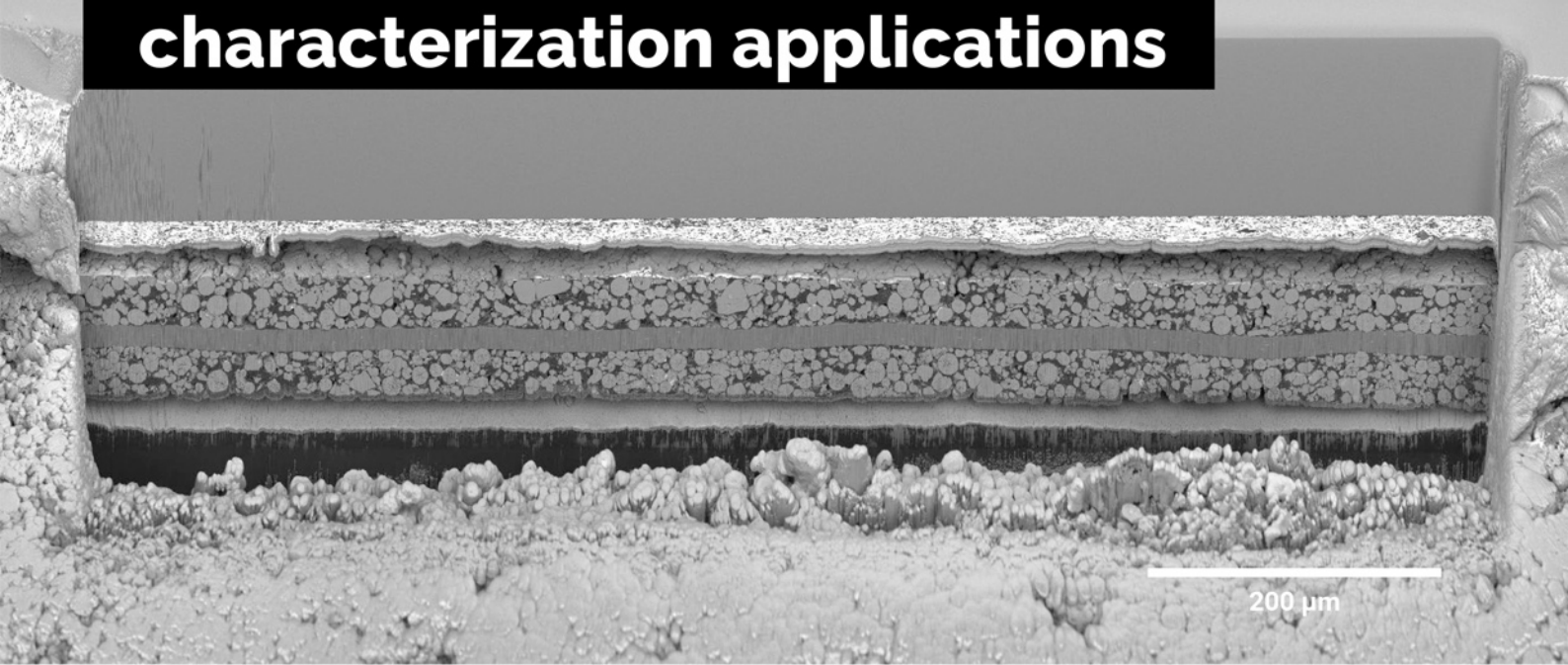


# A unique combination of Plasma FIB and field-free UHR SEM for the widest range of multiscale materials characterization applications



1 mm cross-section through a Li-ion battery electrode

## TESCAN AMBER X

- ✓ High throughput, large area FIB milling up to 1 mm
- ✓ Ga-free microsample preparation
- ✓ Ultra-high resolution, field-free FE-SEM imaging and analysis
- ✓ In-column SE and BSE detection
- ✓ Spot optimization for high-throughput, multi-modal FIB-SEM tomography
- ✓ Superior field of view for easy navigation
- ✓ Essence™ easy-to-use, modular graphical user interface



For more information visit

[www.tescan.com](http://www.tescan.com)

# Graphene Acid for Lithium-Ion Batteries—Carboxylation Boosts Storage Capacity in Graphene

Ievgen Obraztsov, Aristides Bakandritsos,\* Veronika Šedajová, Rostislav Langer, Petr Jakubec, Giorgio Zoppellaro, Martin Pykal, Volker Presser, Michal Otyepka,\* and Radek Zbořil\*


Environmentally sustainable, low-cost, flexible, and lightweight energy storage technologies require advancement in materials design in order to obtain more efficient organic metal-ion batteries. Synthetically tailored organic molecules, which react reversibly with lithium, may address the need for cost-effective and eco-friendly anodes used for organic/lithium battery technologies. Among them, carboxylic group-bearing molecules act as high-energy content anodes. Although organic molecules offer rich chemistry, allowing a high content of carboxyl groups to be installed on aromatic rings, they suffer from low conductivity and leakage to the electrolytes, which restricts their actual capacity, the charging/discharging rate, and eventually their application potential. Here, a densely carboxylated but conducting graphene derivative (graphene acid (GA)) is designed to circumvent these critical limitations, enabling effective operation without compromising the mechanical or chemical stability of the electrode. Experiments including operando Raman measurements and theoretical calculations reveal the excellent charge transport, redox activity, and lithium intercalation properties of the GA anode at the single-layer level, outperforming all reported organic anodes, including commercial monolayer graphene and graphene nanoplatelets. The practical capacity and rate capability of 800 mAh g<sup>-1</sup> at 0.05 A g<sup>-1</sup> and 174 mAh g<sup>-1</sup> at 2.0 A g<sup>-1</sup> demonstrate the true potential of GA anodes in advanced lithium-ion batteries.

## 1. Introduction

The rapidly growing need for electric vehicles and grid electric energy storage, alongside powering portable electronics, calls for energy storage materials that are synthesized from earth-abundant elements, are sustainable and safe, have minimal environmental impact, and give higher performance.<sup>[1,2]</sup> In this context, lithium-ion batteries (LIBs)<sup>[3,4]</sup> have transformed the contemporary energy storage landscape, currently dominating it. The next generation of electrochemical energy storage devices requires removing LIBs' bottlenecks; the cathode materials dictate the capacity of LIBs, with many cathodes being based on non-sustainable Co or Ni elements. Simultaneously, the graphite anodes limit the rate performance and safety due to the slow Li-ion diffusion and operation potential window that is very close to the voltage of Li metal plating. These factors result in rapid graphite anode aging, particularly in power-demanding applications, such as electric

I. Obraztsov, A. Bakandritsos, V. Šedajová, R. Langer, P. Jakubec, G. Zoppellaro, M. Pykal, M. Otyepka, R. Zbořil  
Regional Centre of Advanced Technologies and Materials  
Czech Advanced Technology and Research Institute (CATRIN)  
Palacký University Olomouc  
Šlechtitelů 27, Olomouc 77 900, Czech Republic  
E-mail: a.bakandritsos@upol.cz; michal.otyepka@upol.cz;  
radek.zboril@upol.cz

A. Bakandritsos, R. Zbořil  
Nanotechnology Centre  
Centre of Energy and Environmental Technologies  
VŠB-Technical University of Ostrava  
17. listopadu 2172/15, Ostrava-Poruba 708 00, Czech Republic

 The ORCID identification number(s) for the author(s) of this article can be found under <https://doi.org/10.1002/aenm.202103010>.

© 2021 The Authors. Advanced Energy Materials published by Wiley-VCH GmbH. This is an open access article under the terms of the Creative Commons Attribution License, which permits use, distribution and reproduction in any medium, provided the original work is properly cited.

V. Šedajová, R. Langer  
Department of Physical Chemistry  
Faculty of Science  
Palacký University Olomouc  
17. Listopadu 12, Olomouc 77 900, Czech Republic

V. Presser  
INM – Leibniz Institute for New Materials  
Campus D2 2, 66123 Saarbrücken, Germany

V. Presser  
Department of Materials Science and Engineering  
Saarland University  
Campus D2 2, 66123 Saarbrücken, Germany

V. Presser  
Saarene – Saarland Center for Energy Materials and Sustainability  
Campus C4 2, 66123 Saarbrücken, Germany

M. Otyepka  
IT4Innovations  
VŠB-Technical University of Ostrava  
17. listopadu 2172/15, Ostrava-Poruba 708 00, Czech Republic

DOI: 10.1002/aenm.202103010

vehicles, and impose the risk of catastrophic battery failure due to Li metal dendrites growth.<sup>[5,6]</sup>

Organic materials undergoing reversible electrochemical redox processes and coordinating lithium, are attractive anode candidates in organic/LIBs thanks to their cost-effective and eco-friendly nature, abundance, processability, and design versatility.<sup>[7,8]</sup> Moreover, customized functional groups and heteroatoms in these materials may tune the redox potential, the system's capacity, and the mechanism of charge storage.<sup>[9,10]</sup> Several organic materials have been proposed, embracing conjugated polymers<sup>[11]</sup> and systems bearing carbonyl,<sup>[12,13]</sup> nitrile,<sup>[14]</sup> organosulfur,<sup>[15]</sup> imine,<sup>[16]</sup> azo compounds,<sup>[17,18]</sup> or organic radicals.<sup>[19,20]</sup> Such electrode materials are not restricted by the dimensions of a charge-carrying ion, thus allowing the use of alternatives more sustainable than lithium, such as sodium,<sup>[21,22]</sup> potassium,<sup>[23,24]</sup> zinc,<sup>[25]</sup> magnesium,<sup>[26]</sup> or aluminum.<sup>[27,28]</sup>

Carboxylic acids have emerged as stable and high-energy organic LIB anode materials owing to their low reduction potential and their coordination proclivity toward Li. Di-lithium salts of terephthalic and muconic acids were initially reported as LIB anode active materials.<sup>[29]</sup> Terephthalate could bind 2.3 Li ions per molecule with a reduction potential plateau near 0.8 V, delivering 300 mAh g<sup>-1</sup>. Muconate's performance was about half of that, with its potential plateau being at 1.4 V. Aromatic conjugated carboxyl derivatives demonstrate intramolecular charge delocalization superior to that of non-conjugated derivatives. Consequently, they provide more efficient utilization of carboxyl groups for the storage of lithium ions.<sup>[29–34]</sup>

The capacity of active organic materials can be expressed as the ratio between the number of coordinated Li-ions over the molecular mass of the organic molecule. Therefore, an organic anode active material containing a high percentage of carboxyl groups is extremely desirable for enhancing the capacity. However, the trade-off between imprinting a high content of carboxylic moieties and preserving high conductivity poses a problem, which limits the further development of LIB anode materials. The capacity of most carboxylate active materials known in literature lies below 300 mAh g<sup>-1</sup>.<sup>[29,31–34]</sup> Furthermore, large contents (as high as 50%) of conductive carbon additives in the electrodes are usually required for bypassing the limited conductivity of organic molecules, which however further restrains the practical capacity and commercialization feasibility.<sup>[31,35]</sup>

One way to improve carboxylic acid anodes' performance could be covalent, dense, and spacer-free grafting carboxyls on a highly conductive backbone, such as graphene. In this context, graphene oxide (GO) stands out as a versatile material, bearing a very high amount of various oxygen-containing functionalities<sup>[36,37]</sup> in a complex mixture of tertiary alcohols, epoxides, carboxyl, and carbonyl groups.<sup>[38]</sup> The carboxylic groups in GO represent only a small fraction of the oxygen functionalities (e.g., 1.3 at% by Hummers method)<sup>[39]</sup> located at the edges and around defects.<sup>[39,40]</sup> Unfortunately, the dense functionalization of GO turns it into an insulator, while its reduction enhancing the conductivity leads to a significant loss of the functional groups.<sup>[41]</sup> Another synthetic approach based on graphene functionalization that uses non-covalent interactions<sup>[42]</sup> (e.g.,  $\pi$ - $\pi$ ) is not robust enough for such electrochemical applications because it affords materials with low stability due to leakage of the functionalities into the electrolyte.

Herein, we examine graphene acid (GA, **Figure 1a**), a selectively and densely functionalized carboxylic graphene derivative,

which was thoroughly characterized in previous works,<sup>[43–48]</sup> as a LIB anode. Therefore, we leveraged GA's outstanding functionalization degree of 13 at% (corresponding to more than 30 mass% in carboxylic groups<sup>[48]</sup>), with a sheet resistance of 6800  $\Omega$  sq<sup>-1</sup>, which is five orders of magnitude lower than that of GO.<sup>[43]</sup> GA was prepared from fluorographene by reproducible and up-scalable protocol,<sup>[43,47]</sup> and currently represents the most conductive graphene derivative with such a high content of carboxyl groups. The titration profile of GA closely resembles that of molecular organic acids, with pK<sub>a</sub> of 5.2, reflecting its well-defined structure.<sup>[43]</sup> Thus, GA can be regarded as the first 2D acid. Owing to these features, we can demonstrate that GA, as an organic LIB anode, brings the advantage of i) high redox capacity stemming from its carboxyl groups; ii) high conductivity, boosting the rate capability; iii) high capacity considering the total electrode mass since only 5 mass% of conductive carbon black (CB) additive was used; and iv) extra charge storage due to the co-presence of significant content of *sp*<sup>2</sup> moieties serving as Li intercalation sites (**Figure 1a**). These results indicate that the covalent grafting of carboxyl groups on the conductive skeleton of graphene paves the way for efficient and stable organic anodes for LIBs.

## 2. Results and Discussion

GA was synthesized according to the reported procedure<sup>[43]</sup> described in details in the Experimental, and in the Supporting Information. Briefly, GA was obtained via the selective acidic hydrolysis of cyanographene (G-CN), which was produced from the nucleophilic reaction between [CN]<sup>-</sup> anions and fluorographene,<sup>[43]</sup> a large band-gap 2D *sp*<sup>3</sup> carbon sheet with covalently bonded fluorine atoms. The reaction proceeded replacing of fluorine atoms by -CN groups, accompanied by reductive defluorination, re-establishing the aromatic network and thus the conductivity.<sup>[43]</sup> More details on the chemistry of fluorographene can also be found in other works.<sup>[49–51]</sup> In the following step, a relatively mild acidic hydrolysis selectively transformed the -CN covalent functionalities to -COOH, yielding GA.<sup>[43]</sup> This particular methodology bypasses the harsh oxidation conditions used to introduce diverse oxygen-containing functional groups to graphene during a GO synthesis, and contributed to GA's conductivity, as revealed by conductivity measurements, cyclic voltammetry (CV), electrochemical impedance spectroscopy (EIS), and density functional theory (DFT) calculations.<sup>[43]</sup>

GA electrodes (mixed with Ketjenblack EC-600JD as a conductive additive and polymer binder at a 90:5:5 mass ratio and cast onto a copper current collector) were evaluated in coin cells versus Li metal (Experimental Section). The polymer binder (polyvinylidene fluoride, PVDF) created bridges between the GA microflakes (indicated with arrows in **Figure S1a,b**, Supporting Information, see pure GA in **Figure S1c,d**, Supporting Information), forming a compact electrode architecture with good adhesion between GA's sheets.<sup>[52]</sup> The final electrodes revealed the desirable space filling by conductive nanoparticles of CB (**Figure S2a,b**, Supporting Information), fully preserved even after the electrode's electrochemical operation (**Figure S2c,d**, Supporting Information).

The shapes of the galvanostatic charge-discharge curves (**Figure 1b**) and CV curves (**Figure 1c**) were characteristic for an extended conjugated system with combined redox and

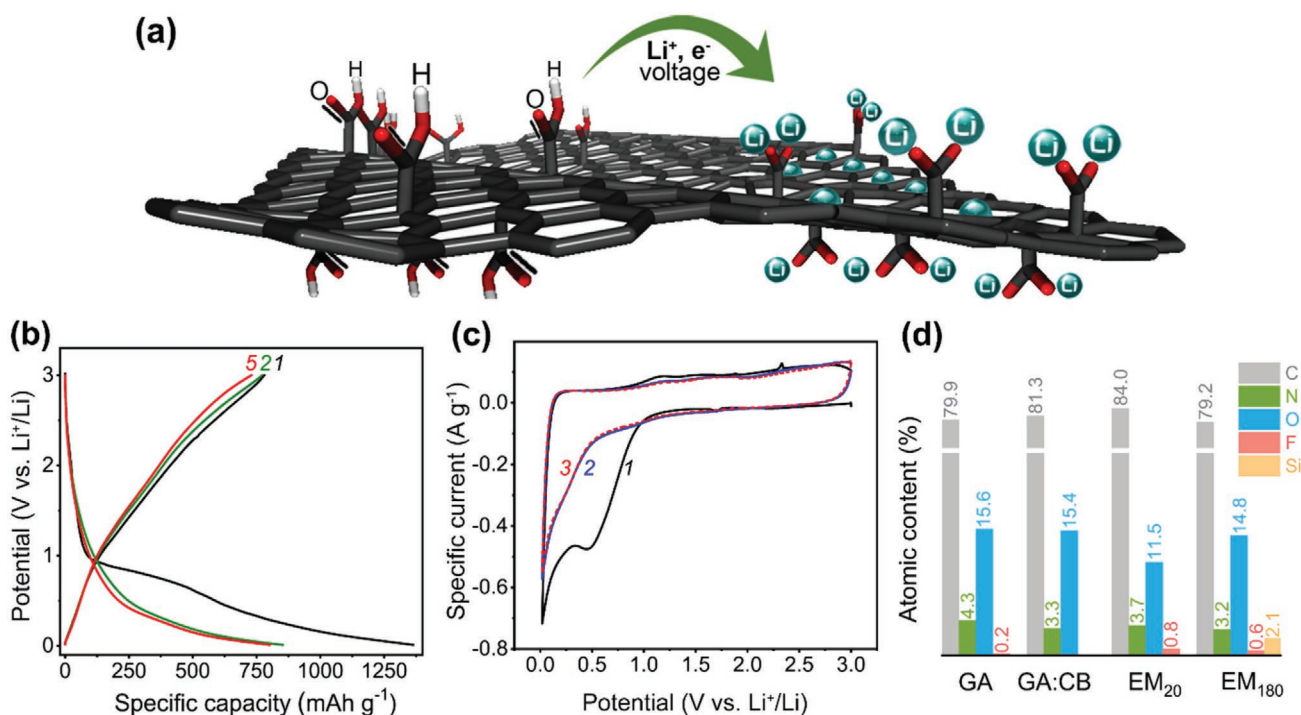


**Figure 1.** a) Schematic representation of GA and its interaction with lithium ions; b) the first, second, and fifth charge–discharge cycle of GA anode in a GA || Li half-cell at 0.05 A g<sup>-1</sup> specific current; c) the three first CV curves for GA anode at a 0.1 mV s<sup>-1</sup> sweep rate (composition GA:CB:PVDF, 90:5:5; cycle number 3 appears as a red-dotted line); and d) relative atomic contents, as obtained from X-ray photoelectron spectroscopy, for pure GA, GA:CB mixture (95:5 by mass), and purified electrode materials after 20 (EM<sub>20</sub>) and 180 (EM<sub>180</sub>) charge-discharge cycles. Si (as SiO<sub>2</sub>) contamination of 2.1 at% after 180 cycles originates from the glass fiber separator; it contributes ≈4% to the oxygen signal.

intercalation energy storage mechanisms.<sup>[53]</sup> Conjugated small molecule carboxylates have sharp reversible redox peaks and distinct plateau during charging and discharging.<sup>[29,54]</sup> However, in GA, a distribution of redox potentials was observed over a wide potential window, as reflected by the smooth redox bands in the range of 1.0–2.0 V versus Li<sup>+</sup>/Li (Figure 1c). This effect was ascribed to the diverse surrounding local environment of the carboxyl groups<sup>[55,56]</sup> bonded on the reconstructed graphene plane after its functionalization, leading to differences in the respective redox potentials (discussed later, in the kinetic redox analysis).

The GA anode (mass loading: 1.0–1.5 mg cm<sup>-2</sup>; thickness: ≈20 μm) delivered a high specific capacity of 747 mAh g<sup>-1</sup> after the first delithiation at 0.05 A g<sup>-1</sup>. The capacity difference between lithiation (1300 mAh g<sup>-1</sup>) and delithiation of the initial cycle (Figure 1b) was due to the proton<sup>[57,58]</sup> and electrolyte reduction with the formation of a solid electrolyte interface (SEI) on the electrode surface.<sup>[59,60]</sup> Therefore, the Coulombic efficiency of the first charge-discharge cycle was 57%, exceeding 90% in the second cycle and finally improving significantly in the successive cycles (>99.4%). The SEI formation was inferred from the voltammogram as an irreversible peak in the first cycle at ≈0.5 V (Figure 1c). Reversible peaks below 0.5 V versus Li<sup>+</sup>/Li in the successive cycles correspond to lithium-ion insertion into graphene.

The composition-based capacity of GA was calculated for a better understanding and interpretation of the experimentally obtained values. For that, the elemental analysis of GA was obtained by X-ray photoelectron spectroscopy, showing

79.9 at%, 4.3 at%, and 15.6 at% of C, N, and O atoms, respectively, along with a trace amount of fluorine atoms (Figure 1d and Figure S3, Supporting Information). The determined atomic content of carboxylic carbons according to C 1s deconvolution was 8 at% (Figure S4 and Table S1, Supporting Information), which translates into 16 at% in oxygen content, because every carboxylic carbon has two oxygen atoms. Since the oxygen content according to the elemental XPS analysis is 15.6 at% (Figure S3b, Supporting Information), the carboxylic carbons alone represent all the oxygen in GA. The 4.3 at% of nitrogen incorporated into graphene, mostly in pyridinic and pyrrolic configurations, originated from the solvent dimethylformamide reactivity.<sup>[43]</sup> Considering the C(sp<sup>3</sup>)-COOH moieties and the surrounding carbon sp<sup>2</sup> area as a single Li-host ensemble, the composition-based capacity of GA was calculated (Figure S4e and Table S1, Supporting Information) for different numbers of coordinated and intercalated Li atoms. The composition-based capacity was 706 mAh g<sup>-1</sup> for reversible binding of four Li atoms per one carboxylic-sp<sup>2</sup> area (Note S1, Supporting Information). These values strongly corroborate (discussed later) the experimentally determined capacity in the rate test (800 or 700 mAh g<sup>-1</sup> at 0.05 A g<sup>-1</sup> for the 5th and 10th cycle, respectively), as well as the computation results on the lithium-ion storage mechanism.

The current–rate performance of the GA electrode was tested at current densities ranging from 0.05 to 2.0 A g<sup>-1</sup> (Figure 2a,b) with capacity ranging from 700 to 174 mAh g<sup>-1</sup>, respectively (10th cycle of each rate). These values correspond to the binding of four and one Li<sup>+</sup> per carboxylic-sp<sup>2</sup> area, respectively

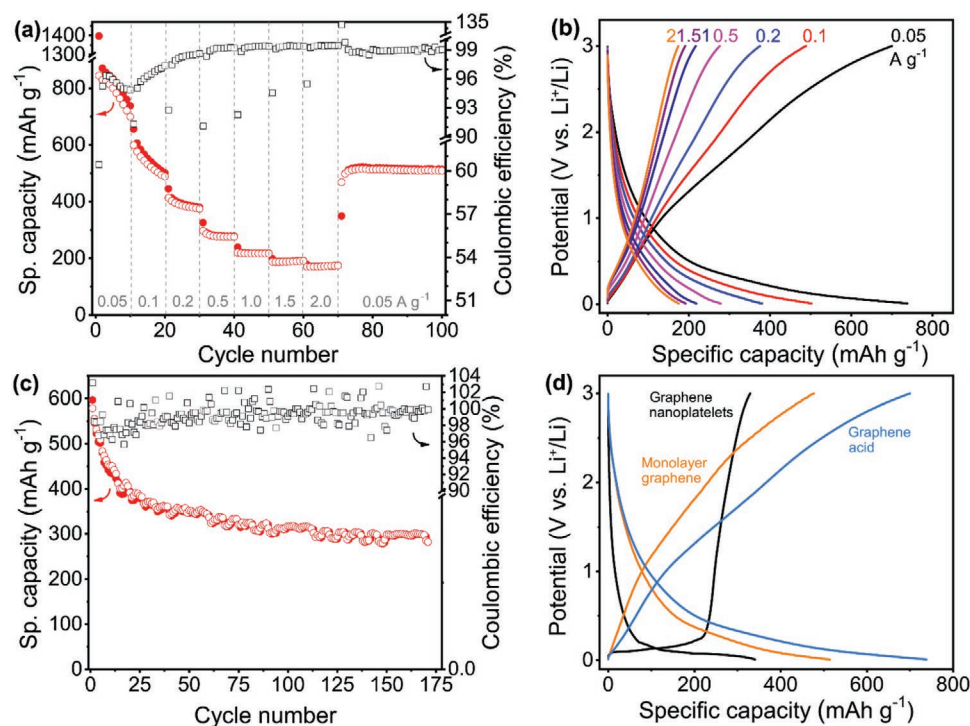


**Figure 2.** Electrochemical testing of GA in half-cell versus Li: a) rate capability test; b) 10th charge-discharge curve for each current density, from the rate test of panel (a); c) cycling performance at  $0.2 \text{ A g}^{-1}$  after one-cycle at  $0.05 \text{ A g}^{-1}$  at  $24 \pm 2 \text{ }^\circ\text{C}$ , and d) the comparison of GA with anodes consisting of monolayer graphene and graphene nanoplatelets at  $0.05 \text{ A g}^{-1}$  (5th cycle), measured under identical conditions. In panels (a) and (c) open symbols represent lithiation and filled symbols represent delithiation.

(Note S1 and Table S5, Supporting Information). Then, the electrode was cycled again at  $0.05 \text{ A g}^{-1}$ , recovering a capacity of  $510 \text{ mAh g}^{-1}$ . The recovered capacity remained stable for 30 consecutive cycles with the Coulombic efficiency exceeding 99% (Figure 2a). Comparatively, polymeric carboxylic anodes severely suffered from slow Li-ion diffusion at higher current rates, exhibiting  $500 \text{ mAh g}^{-1}$  and  $50 \text{ mAh g}^{-1}$  at  $0.05 \text{ A g}^{-1}$  and  $2 \text{ A g}^{-1}$ , respectively.<sup>[61]</sup> The advantage of GA is also clearly observed comparing its operation with a (carboxylic acid)-modified reduced GO anode (rGO-poly(methyl methacrylate)), which delivered  $\approx 170 \text{ mAh g}^{-1}$  at  $0.1 \text{ A g}^{-1}$ .<sup>[62]</sup> The specific capacity and the Coulombic efficiency of GA anodes were reproducible in the subsequent electrode material preparations, even under different mass loadings (Figure S5a,b, Supporting Information). The average delithiation voltage advantageously decreased from 1.83 to 1.47 V at higher current rates (Figure S6, Supporting Information) because of a change in the ratio of diffusion- to surface-controlled capacity components.

After the initial 20 cycles of the stability test at  $0.2 \text{ A g}^{-1}$ , the GA anode's specific capacity was  $400 \text{ mAh g}^{-1}$  and then gradually reduced to  $300 \text{ mAh g}^{-1}$  during the consecutive 150 cycles (Figure 2c). After 180 galvanostatic charge/discharge cycles (stability testing) and CV at different rates, the GA electrode recovered a specific capacity of  $475 \text{ mAh g}^{-1}$  when cycled back at  $0.05 \text{ A g}^{-1}$ . This behavior demonstrates the high repeatability and stability of its electrochemical properties (Figure S7, Supporting Information).

Examination via X-ray photoelectron spectroscopy was also performed in order to better understand the electrochemical

behavior of GA during cycling. The GA material was collected from the electrodes after 20 and 180 cycles of the stability test at  $0.2 \text{ A g}^{-1}$  and was purified from the electrolyte and the polymer binder. The oxygen content after 20 cycles decreased from 15.4 to 11.5 at% (Figure S1d, Supporting Information), corroborating the similar decrease in carboxyl groups from 8 to 5.2 at% (Figure S4, Supporting Information). The decline in the oxygen content occurred during the first 20 cycles. The structure remained practically unchanged for the following 180 cycles; this may be attributed to the reduction of some carboxyl groups during SEI formation.

The performance of the GA anode was compared to anodes made of graphene from commercial suppliers: i) graphene nanoplatelets dispersed in 1-methyl-2-pyrrolidinone (ACS Materials) containing flakes of 1–3  $\mu\text{m}$  in diameter and 3–5 nm in thickness, and ii) monolayer (99.8%) graphene powder (Ossila) containing flakes of  $\approx 2 \mu\text{m}$  in diameter and 0.7–1.2 nm in thickness. The specific capacity of graphene anodes after the fifth cycle at  $0.05 \text{ A g}^{-1}$  was 476 and 330  $\text{mAh g}^{-1}$  for monolayer graphene and graphene nanoplatelets, respectively. These values were significantly lower than that of GA ( $800 \text{ mAh g}^{-1}$ , Figure 2d). The charging/discharging of graphene nanoplatelets was found similar to that expressed by small-crystal graphite<sup>[63]</sup> (indicating its multilayered nature) and suffered from severe capacity decay to  $\approx 50 \text{ mAh g}^{-1}$  at  $1.5 \text{ A g}^{-1}$  (Figure S8a, Supporting Information). The monolayer graphene performed better, keeping  $250 \text{ mAh g}^{-1}$  at  $1.5 \text{ A g}^{-1}$  (Figure S8b, Supporting Information). The GA anode at comparable electrode material loading delivered higher capacity than monolayer graphene at

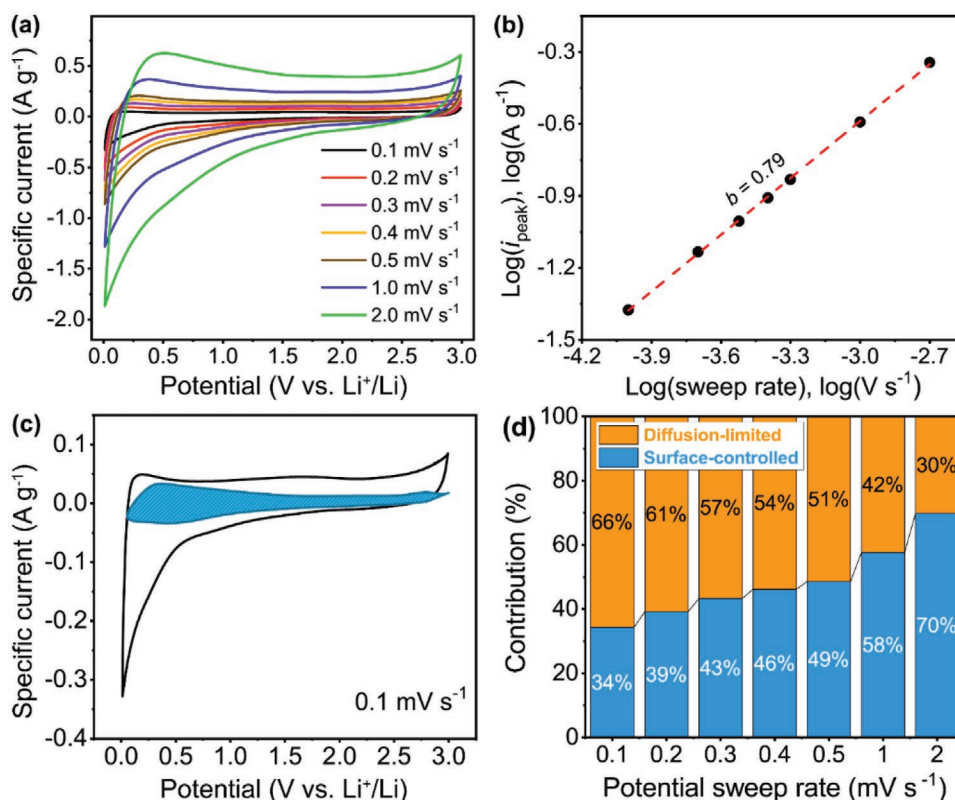


**Figure 3.** a) CV curves for GA at different scan rates performed after the life-cycle test, b) The linear curve from Equation (1) for the determination of the  $b$ -value at 1.27 V and at the potential sweep rate range of 0.1–2.0  $\text{mV s}^{-1}$ , c) CV curve for GA anode showing the fractions corresponding to surface capacity (shaded region) and redox processes, at 0.1  $\text{mV s}^{-1}$ , d) Contribution of diffusion- and surface-controlled processes on the capacity of the GA anode at different potential sweep rates.

all current rates (Figure S8c, Supporting Information), which is particularly interesting considering the much higher conductivity of pristine graphene. The performance of GA was also compared against maleic acid<sup>[64–66]</sup> anodes (Figure S9, Supporting Information), which were prepared following the published protocols and using a range of different carbon additives, further highlighting the superior performance of GA.

To experimentally determine the contribution of the diffusion-limited and surface-controlled charge storage mechanisms arising from the carboxylic groups and graphene moieties, respectively, an electrochemical kinetic analysis was performed.<sup>[67]</sup> The CV curves were recorded at different scan rates (Figure 3a) after the 180-cycle stability test. Using equation  $i_p = a\nu^b$  and plotting the logarithm of the peak current ( $i_p$ , for the 1.27 oxidation peak) versus the logarithm of the scan rate  $\nu$  (Figure 3b), the  $b$  value was calculated from the slope. Many advanced materials show a mixed behavior with intermediate values. In the present case, a  $b$ -value of 0.79 was obtained. Such a value reflects the excellent rate handling ability of GA anodes owing to the high conductivity of GA and the surface-exposed -COOH groups where the diffusion-controlled processes mostly operate.

When the  $k_1$ - $k_2$  model is employed, the purely diffusion-limited and purely surface-controlled contributions to the overall current response can be separated. Equation (1) separates the total current, which can be presented as the sum of surface capacitive ( $k_1\nu$ ) and of diffusion-limited ( $k_2\nu^{1/2}$ ) processes components:

$$i = k_1\nu + k_2\nu^{1/2} \text{ or } i(\nu) / \nu^{1/2} = k_1\nu^{1/2} + k_2 \quad (1)$$

where,  $k_1$  and  $k_2$  are potential sweep rate-independent values. These values for fixed potentials were determined from the slope and y-axis intercept point from the  $i/\nu^{1/2}$  versus  $\nu^{1/2}$  plot, respectively (Figure S10a,b, Supporting Information).

The total currents during CV at each potential sweep rate were deconvoluted accordingly (Figure S11, Supporting Information), showing that the diffusion-limited current fraction (66% at 0.1  $\text{mV s}^{-1}$ ) of the electrode was substantially higher than the one estimated from the stoichiometry of GA (24%). This suggests significant redox contribution from the GA radical sites<sup>[48]</sup> and N-doped centers.<sup>[68]</sup>

The fraction of the diffusion-limited current, most likely linked to the redox process from GA surfaces, decreased to 30% when the scan process from GA increased to 2.0  $\text{mV s}^{-1}$  (Figure 3d). The same analysis performed for a freshly assembled half-cell (Figure S12a–c, Supporting Information) showed similar electrochemical performance but with a higher fraction of diffusion-limited processes at each potential sweep rate. The  $b$ -value was 0.72 in this case, in line with the larger contribution of diffusion-limited processes, reaching 75% at 0.1  $\text{mV s}^{-1}$  and 37% at 2  $\text{mV s}^{-1}$ .

The charge–discharge transient at 0.05  $\text{A g}^{-1}$  in the form of differential capacity versus voltage plot allowed the delineation of the different electrochemical processes at the whole potential

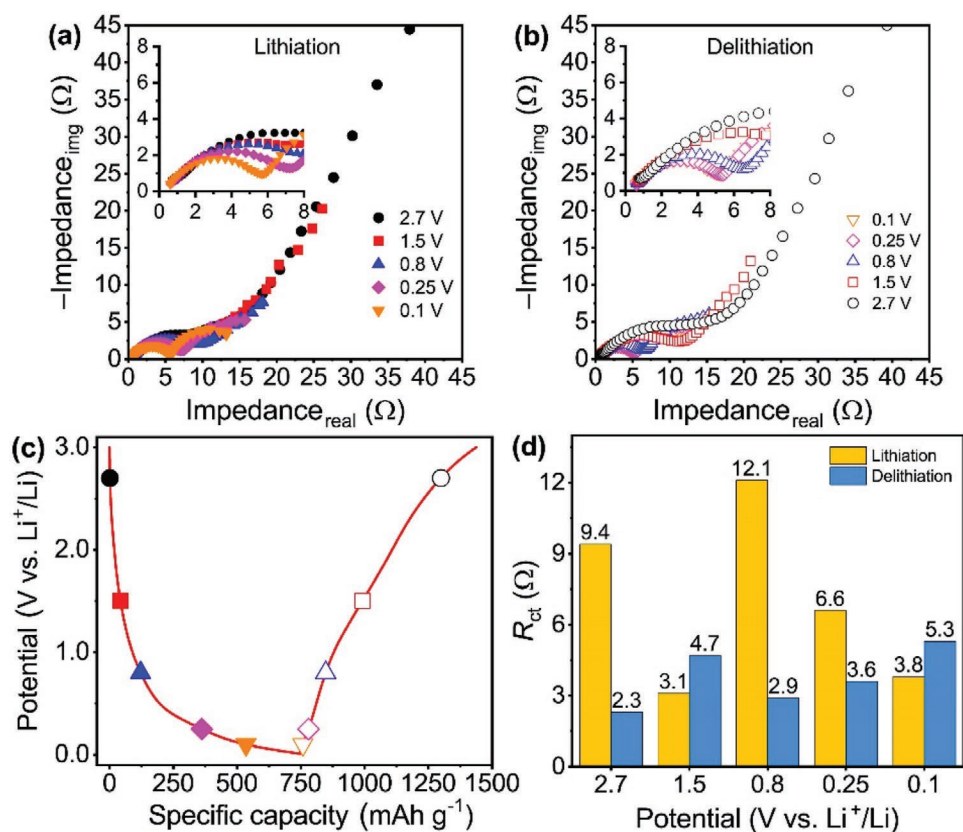


**Figure 4.** EIS spectra for the GA anode against Li, galvanostatically recorded at specific voltages during a) lithiation and b) delithiation, c) charge–discharge curve with indicated voltages where EIS is performed, and d)  $R_{ct}$  dependence on state of charge and discharge of the cell.

region (Figure S13, Supporting Information). Three broad redox peaks were distinguishable: below 0.5, between 1.0 and 2.0 V, and above 2.5 V versus  $\text{Li}^+/\text{Li}$ . The first one corresponds to lithiation–delithiation of the  $sp^2$  graphene moieties of GA. The second is a typical region for carboxylate redox reactions;<sup>[9]</sup> the third could be regarded as redox-processes involving nitrogen-containing graphene moieties<sup>[68]</sup> introduced during the synthesis (Figures S3 and S4, Supporting Information).

As previously identified, GA showed a very high rate capability. To better understand this property, Nyquist plots were obtained from electrochemical impedance spectroscopy (EIS) measurements at different discharge states of the GA electrode (Figure 4a–c). Fitting Nyquist plots with a modified Randles circuit (Figure S14, Supporting Information) showed very low charge transfer resistance ( $R_{ct}$ ) values in the entire voltage (Figure 4d). These values were significantly lower in comparison with dozens or hundreds of ohms typically observed for previously reported carboxyl-based organic anodes (Table S3, Supporting Information).<sup>[54,55,62]</sup> The low  $R_{ct}$  value verifies and highlights the fast kinetics of the carboxyls' group redox process and the high electronic charge transfer offered from the conductive graphenic backbone corroborating the initial hypothesis. Specifically, the lowest  $R_{ct}$  values for GA were 3.1 and 2.9  $\Omega$  on lithiation (discharge) and lithiation (charge) of the half-cell at 1.5 and 0.8 V versus  $\text{Li}^+/\text{Li}$ , respectively, unveiling GA's beneficial properties.

Operando Raman spectra were recorded every  $\approx 250$  mV during CV at 0.05  $\text{mV s}^{-1}$  potential sweep rate (Figure 5a) to

shed more light on the Li storage processes in the GA anode. Raman spectra revealed that the G-band position was red-shifting during the charging of the GA anode due to the biaxial tensile strain in GA. It is known that the red-shift in the G-band below 0.5 V is more pronounced as the number of graphene layers in a stack decreases.<sup>[69]</sup> For example, a G-band position shift of 3, 5, and 11  $\text{cm}^{-1}$  was found for 100 nm graphite particles, 20 nm graphite flakes, and 3-layer graphene nanoplatelets, respectively. The G-band of GA was shifted by  $\approx 18$   $\text{cm}^{-1}$  in the 0.5–0.09 V region (Figure 5b), which is larger than that of a few-layer graphene material. This indicates that extensive interactions of Li atoms with GA take place at the single-layer level. In the plot of the G-band position versus potential, three slopes were observed during lithiation ( $\approx$  in the 3.0–2.0, 2.0–0.75, and 0.75–0.09 V range, Figure 5b) instead of two slopes observed for graphene.<sup>[69]</sup> In particular, the additional slope between  $\approx 2.0$ –0.75 V probably reflects the mechanism of Li storage involving the carboxyl groups of GA. This is strongly corroborated by the voltage ranges very similar to those observed in the CV kinetic analysis (Figure 3) and the differential capacity analysis (Figure S13, Supporting Information), which was ascribed to a lithium-ion interaction with the graphene moieties (3.0–2.0 V), as well as to carboxylate redox reactions with Li (2.0–0.5 V) and Li interactions with nitrogen-containing  $sp^2$  areas (0.5–0.01 V). Finally, Raman results also showed that the  $I_D/I_G$  ratio grew during the lithiation of GA to  $\approx 0.5$  V, where a knee was observed (Figure 5c). The increase of the  $I_D/I_G$  ratio is

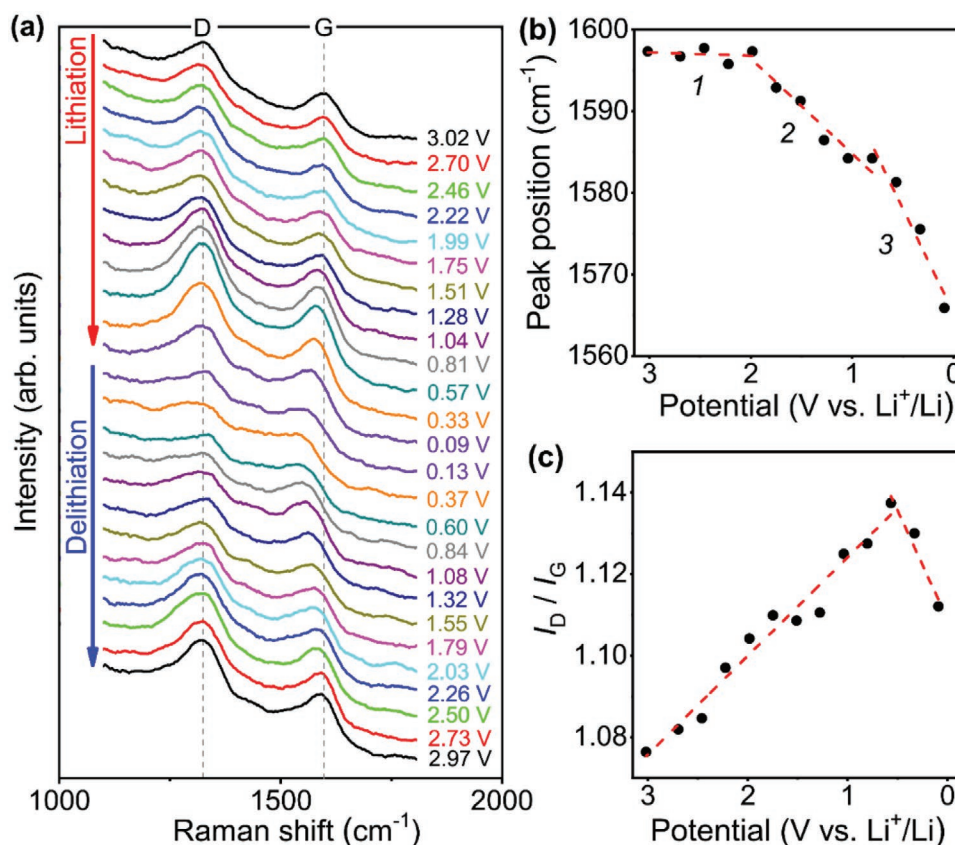


**Figure 5.** a) Operando Raman spectra of GA anode recorded at different potentials during CV at potential sweep rate of  $0.05 \text{ mV s}^{-1}$ , b) G-band position at different potentials, and c) D-to-G peak intensity ratio during lithiation.

associated with lowering the Fermi level<sup>[70]</sup> caused by n-doping during the negative polarization of the GA electrode followed by the reduction of  $\text{Li}^+$  to  $\text{Li}^0$  and a free carrier concentration decrease in the GA, causing an abrupt change (the knee) in this potential (Figure 5c).

Theoretical calculations using both finite (functionalized ovalene) and infinite (periodic) models were carried out for a better understanding of the energy storage mechanism in GA. The calculations show that up to 4  $\text{Li}^0$  atoms per one carboxyl group (Figure 6) can be bound to GA (with adsorption energy

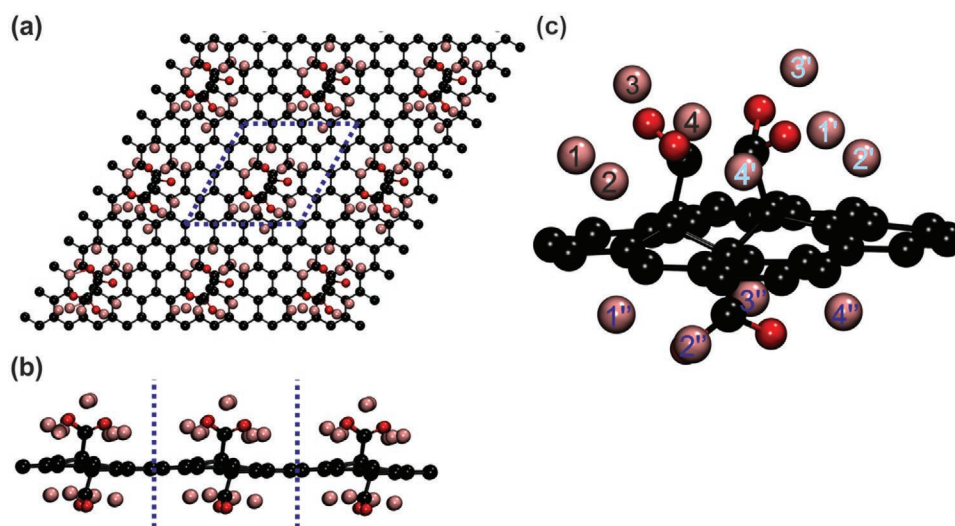


**Figure 6.** A model of lithiated GA according to DFT calculations; a) top and b) side views (the dashed line dictates the super-cell used in calculations). The zoom view c) shows two binding modes of Li atoms close to one (bottom) and two (up) carboxyl groups (C, O, and Li atoms are shown as black, red, and pink, respectively, balls). The atom numbering is arbitrary to highlight up to four Li atoms close to the nearest carboxyl group.



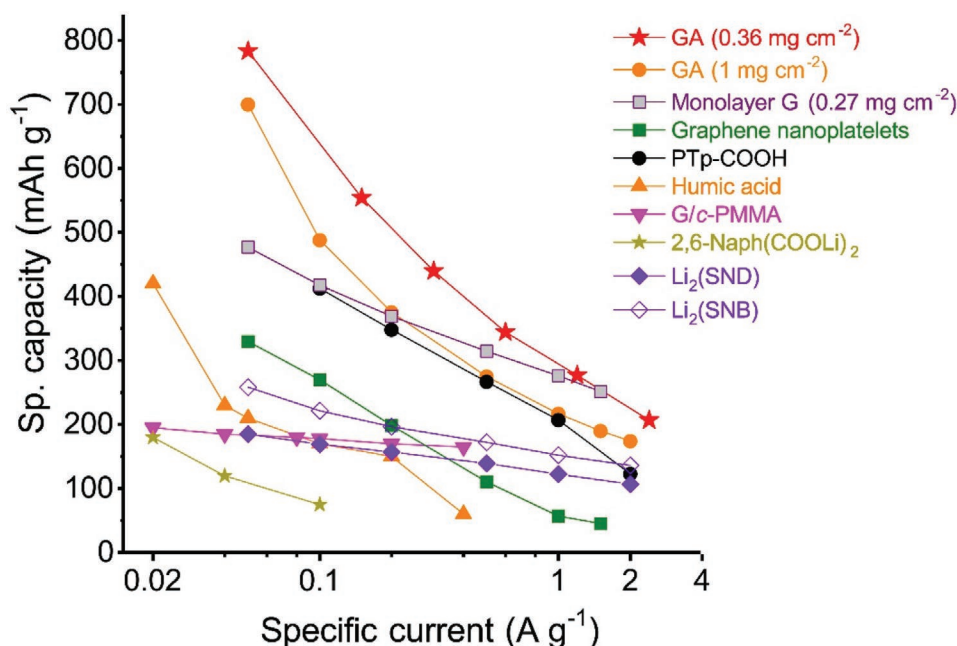


**Figure 7.** Performance comparison of organic materials from Table S4, Supporting Information: PTP-COOH,<sup>[61]</sup> humic acid,<sup>[71]</sup> G/c-PMMA,<sup>[62]</sup> 2,6-Naph(COOLi)<sub>2</sub>,<sup>[72]</sup> Li<sub>2</sub>(SND), Li<sub>2</sub>(SNB),<sup>[55]</sup> and electrodes prepared using commercial graphene (monolayer, and nanoplatelets). Capacity values are normalized to the total mass of electrode materials and refer to the stabilized capacity in the current rate tests.

of  $-576 \text{ kcal mol}^{-1}$  per Li<sup>0</sup> atom) without significant structural changes. The Li<sup>0</sup> atoms prefer to bind close to carboxyl group adopting two binding modes: the Li atom is either in contact both with the  $sp^2$  carbon area and the carboxyl oxygens or, the Li atom binds between the carboxyl oxygens (Figure 6). These findings are in line with the composition-based GA capacity calculation (Note S1 and Table S5, Supporting Information) and with the experimentally determined capacity of GA (Figure 2a), suggesting the same ratio of four Li atoms per carboxyl with its respective  $sp^2$ -hybridized carbon lattice area. Such excellent agreement of the theoretical results (based on single sheet model of GA) with the experiments supports the operation of GA on the single-layer level, as Raman investigations also unveiled. According to calculations, the addition of a fifth Li atom per carboxyl is not favored, because it has positive adsorption energy. Also, Li<sup>+</sup> ions have weaker bonding to GA than Li<sup>0</sup>, thus allowing their easy migration to the cathode (Note S2, Supporting Information), as required during the discharging. Finally, in both oxidized/reduced states, the partial charge on Li is  $\approx 0.94\text{--}0.99 e$  (see S2, Supporting Information), which indicates strong charge transfer processes between the Li species and the GA skeleton and is attributed to the linker-free installation of the carboxyl groups on the  $sp^2$  backbone.

The performance of GA anode is found superior to most of the polymer, oligomer, composite and small-molecule, and carboxyl anodes, both at low and higher specific currents (Figure 7 and Table S4, Supporting Information). For example, the capacity of a carboxyl modified polythiophene (PTP-COOH) electrode material was  $\approx 500 \text{ mAh g}^{-1}$  at  $0.05 \text{ A g}^{-1}$ ; however, at high rates, the film gave only  $50 \text{ mAh g}^{-1}$  at  $2 \text{ A g}^{-1}$ .<sup>[61]</sup> A humic acid anode showed a capacity of  $\approx 420 \text{ mAh g}^{-1}$  and  $20 \text{ mAh g}^{-1}$  at  $0.06 \text{ A g}^{-1}$  and  $0.4 \text{ A g}^{-1}$ , respectively.<sup>[71]</sup> An electrode made

from graphene chemically cross-linked with poly(methyl methacrylate) (Gr/c-PMMA composite) delivered  $250 \text{ mAh g}^{-1}$  and  $167 \text{ mAh g}^{-1}$  at  $0.02 \text{ A g}^{-1}$  and  $0.4 \text{ A g}^{-1}$ , respectively.<sup>[62]</sup> Small-molecule carboxylic anodes, such as terephthalate, mucate,<sup>[29]</sup> 2,5-dihydroxyterephthalic acid,<sup>[32]</sup> 2,6-naphthalene dicarboxylate,<sup>[33]</sup> 4,4'-(phenazine-5,10-diyl)dibenzoate,<sup>[34]</sup> demonstrated only moderate capacities ( $\leq 300 \text{ mAh g}^{-1}$ ) because of the low ratio between stored lithium ions and molar mass (Table S4, Supporting Information).

Although graphene anode was reported to possess a  $650 \text{ mAh g}^{-1}$  capacity after the 1st delithiation,<sup>[73]</sup> this value was reached under undefined mass loading and temperature conditions. Accordingly, we tested two commercial graphene samples under conditions identical to GA. As described earlier, of these two materials, one had a very high content of monolayer sheets and the other showed multilayered nature. As demonstrated by our data, the GA anode outperformed these reference materials. The advantage of GA lies in its conductivity combined with a high content in carboxyl groups, delivering a capacity and rate performance that is unmatched by any value expressed by the wide gamut of carboxyl-based organic LIB electrodes, as highlighted in the comparative graph in Figure 7 and Table S4, Supporting Information.

### 3. Conclusions

Graphene-acid (GA, a densely functionalized carboxylated graphene) is a very effective LIB anode material by combining redox and intercalation properties, originating from the conductive and selectively carboxylated 2D graphene backbone. Due to the spacer-free carboxyl groups attached to graphene's

lattice, which allowed their direct communication with the graphene backbone, the anode was endowed with particularly low charge transfer resistance, and effective interactions and intercalation of lithium-ions. Operando Raman, as well as theoretical results, indeed verified that GA behaved as a high-quality monolayer graphene. Further, calculations confirmed a direct charge communication pathway between the Li atoms/ions and the GA host, with the experimental and composition-based capacities being in agreement with the theoretically calculated capacities. The carboxylic groups of GA coordinated the lithium ions upon the electroreduction in a broad potential range (in contrast to small molecule materials). Simultaneously, the graphene skeleton served concurrently as a highly conducting backbone, redox, and intercalation electrode material. Therefore, overall, the GA anode worked better than polymeric, oligomeric, and molecular carboxylated anodes and few-layered and monolayer graphene in terms of the capacity as well as the rate performance. The particularly competitive performance of GA, alongside its highly reproducible and scalable synthesis, predisposes this material for efficient application as a LIB anode.

#### 4. Experimental Section

**Chemicals:** Fluorographite, DMF, 1-methyl-2-pyrrolidinone, bulk solvents, PVDF, battery-grade 1.0 M LiPF<sub>6</sub> ethylene carbonate: dimethyl carbonate (EC:DMC, 1:1 by volume) electrolyte solution, and Whatman GF/A glass microfiber filters were purchased from Sigma-Aldrich. The 0.75 mm-thick lithium metal foil (99.9%) was from Alfa Aesar; CB (Ketjenblack EC-600JD) was supplied by AkzoNobel Functional Chemicals BV. Monolayer graphene powder (M901, 99.8% single layer ratio, >99% purity) was from Ossila Ltd.; graphene nanoplatelets NMP dispersion of 98.9% purity was from ACS Material. All reagents were used as received.

GA was synthesized according to the literature procedure.<sup>[43]</sup> In brief: commercial fluorographene powder was dispersed in DMF followed by adding NaCN and stirring at 130 °C. The resulting cyanographene was separated, washed, and deionized by dialysis. Next, cyanographene was hydrolyzed with a nitric acid solution to form GA water dispersion. The GA was washed in successive separation-dispersion cycles and freeze-dried. Detailed synthesis is provided in the Supporting Information, along with transmission electron microscopy and atomic force microscopy (AFM) results (Figure S15, Supporting Information).

**Materials Characterizations:** XPS post-mortem analysis of electrodes was performed by PHI VersaProbe II (Physical Electronics) spectrometer using an Al-K $\alpha$  source (15 kV, 50 W). The obtained data were evaluated with the MultiPak (ULvac-PHI) software package. The electrode materials were washed in several consecutive redispersion-separation cycles in NMP, hot DMF, 1 mM HCl, and ethanol (twice in each solvent) in order to remove the electrolyte, polymer binder, and residual SEI components. Raman spectra were recorded by using DXR Raman Microscope (Thermo Fisher Scientific) using 633 nm excitation line diode laser with an aperture of 50  $\mu$ m, 5 cm<sup>-1</sup> resolution and MTI electrochemical cell with a quartz window for Raman analysis, a GA:PVDF (90:10 by mass) film was cast onto a Ni foam. Transmission electron microscopy images were obtained with a JEOL 2100 system. For these analyses, a droplet of GA dispersion in ultrapure water (concentration approximately 0.1 mg mL<sup>-1</sup>) was placed on a holey carbon-coated copper grid and left to dry, before the analysis. AFM images were obtained in the amplitude-modulated semi-contact mode on an NT-MDT NTegra system equipped with a VIT-P AFM probe using freshly cleaved muscovite mica as a substrate.

**Electrode Preparation and Cell Assembling:** The active material, the carbon additive, and the binder were mixed in the 90:5:5

(GA:carbon black:polymer binder) weight ratio. The composition of the reference commercial graphene electrodes was ACS Materials graphene nanoplatelets:PVDF (95:5 by mass) and Ossila monolayer graphene:PVDF (80:20 by mass). A higher binder content in a monolayer graphene anode was required for preparing physically stable film on the current collector foil. Individual components were dispersed separately by ultrasonication in a suitable amount of NMP and then mixed in a Thinky ARV-310 planetary mixer (Thinky Co.) for 5 min at 1100 rpm under pressure decreased to 30 kPa. The slurry was cast onto a 10- $\mu$ m thick copper foil (Cambridge Energy Solutions) with a doctor blade using 100- $\mu$ m slot. The film was dried with an infrared lamp for 10 min, left overnight in a vacuum oven at 120 °C, and then cut into 15-mm disks, which were used for CR2032 and research-grade coin cells (PAT-cell of EL-Cell GmbH) assembling in a dry Ar-filled glove box ([O<sub>2</sub>] < 0.6, [H<sub>2</sub>O] < 0.8 ppm). Lithium metal coin (15.5 mm diameter, 0.75 mm thickness), glass microfiber separator, and 1.0 M LiPF<sub>6</sub> EC:DMC (1:1 vol.) were used as the counter electrode, the separator, and the electrolyte (100  $\mu$ L), respectively. The lithium metal surface was mechanically refreshed before cell assembling. The electrode material loading was 1.0–1.5 mg cm<sup>-2</sup> unless otherwise specified.

**Electrochemical Measurements:** CV experiments were performed using a BCS-810 system under BT-lab software control of BioLogic Science Instruments; charge-discharge rate and stability tests were performed using Novonix HPC setup with a dedicated thermostatic chamber (Novonix) at 25 °C. The cells were tested at 3.0–0.01 V versus Li<sup>+</sup>/Li. The mass of all electrode material components was used for specific capacity calculations. All cells were discharged to 3.0 V by a CC-CV (constant current-constant voltage) procedure after assembling in order to prevent Cu collector oxidation, followed by a 6-h rest at OCP and charging back to 3.0 V (Figure S16a, Supporting Information). One charge–discharge cycle at 0.05 A g<sup>-1</sup> was performed (Figure S16b, Supporting Information) before the stability test reported in Figure 3c. EIS measurements were performed in a three-electrode PAT-Cells (EL-Cell GmbH) with a Li reference ring electrode using Metrohm Autolab PGSTAT128N potentiostat equipped with FRA32M extension card under Nova 1.11.2 control and analysis software (Metrohm Autolab BV). The GA electrode material was aged for 10 cycles at 0.05 A g<sup>-1</sup>, followed by two cycles with a fresh Li metal coin (Figure S17, Supporting Information). The EIS was performed at different states of charge of the cell in a galvanostatic mode; 50  $\mu$ A AC oscillation amplitude over the frequency range of 0.3 Hz to 100 kHz was used.

**Computational Methods:** The infinite (periodic) calculations were performed by using spin-polarized DFT as implemented in a Vienna Ab-initio Simulation Package.<sup>[74–76]</sup> The electron-ion interactions were treated by a projector-augmented wave (PAW) method,<sup>[77,78]</sup> and the Perdew, Burke, and Ernzerhof functional<sup>[79]</sup> in the generalized gradient approximation and Grimme D2 dispersion.<sup>[80]</sup>

The basis set contained plane waves with a maximum kinetic energy of 500 eV and a  $\Gamma$ -centered  $6 \times 6 \times 1$  *k*-point mesh. All structures were optimized until the forces acting on all atoms were reduced to less than 10 meV  $\text{Å}^{-1}$  and the electronic and magnetic degrees of freedom were relaxed until the change in total energy between the successive iteration steps was smaller than 10<sup>-6</sup> eV.

The adsorption energy,  $E_{ad}$ , per lithium atom was evaluated as

$$E_{ad} = 1/n(E_{GA+nLi} - E_{GA-nLi} - nE_{Li}) \quad (2)$$

where  $E_{GA+nLi}$ ,  $E_{GA-nLi}$  and  $E_{Li}$  stands for total energies of whole GA-lithium system, system without lithium atom and lithium atom, respectively.  $n$  denotes the number of lithium atoms (Figures S18 and S19, Supporting Information).

#### Supporting Information

Supporting Information is available from the Wiley Online Library or from the author.

## Acknowledgements

The work was supported by the ERDF/ESF project “Nano4Future” (No. CZ.02.1.01/0.0/0.0/16\_019/0000754). R.Z. and A.B. acknowledge the funding from the Czech Science Foundation, project GA CR – EXPRO, 19–27454X. V.Š. and R.L. thanks the Internal Student Grant Agency of the Palacký University in Olomouc, Czech Republic (IGA\_PrF\_2021\_031). M.O. acknowledges the ERC grant 2D-CHEM, No 683024 from H2020. V.P. thanks Eduard Arzt (INM) for continuing support. Operation of XPS and TEM facilities was partly funded by the Research Infrastructure NanoEnviCz, supported by the Ministry of Education, Youth and Sports of the Czech Republic under Project No. LM2018124. The authors thank E. Ioannou for SEM measurements.

## Conflict of Interest

The authors declare no conflict of interest.

## Data Availability Statement

The data that support the findings of this study are available from the corresponding author upon reasonable request.

## Keywords

carboxylation, graphene acid, lithium-ion batteries, organic anodes

Received: September 27, 2021

Revised: December 1, 2021

Published online: December 22, 2021

- [1] A. R. Dehghani-Sanij, E. Tharumalingam, M. B. Dusseault, R. Fraser, *Renewable Sustainable Energy Rev.* **2019**, *104*, 192.
- [2] Y. Yang, E. G. Okonkwo, G. Huang, S. Xu, W. Sun, Y. He, *Energy Storage Mater.* **2021**, *36*, 186.
- [3] G. E. Blomgren, *J. Electrochem. Soc.* **2017**, *164*, A5019.
- [4] M. Li, J. Lu, Z. Chen, K. Amine, *Adv. Mater.* **2018**, *30*, 1800561.
- [5] Q. Zhang, W. Cai, Y. X. Yao, G. L. Zhu, C. Yan, L. L. Jiang, C. He, J. Q. Huang, *Chem. Soc. Rev.* **2020**, *49*, 3806.
- [6] P. Zhang, T. Yuan, Y. Pang, C. Peng, J. Yang, Z.-F. Ma, S. Zheng, *J. Electrochem. Soc.* **2019**, *166*, A5489.
- [7] Y. Lu, J. Chen, *Nat. Rev. Chem.* **2020**, *4*, 127.
- [8] P. Poizot, J. Gaubicher, S. Renault, L. Dubois, Y. Liang, Y. Yao, *Chem. Rev.* **2020**, *120*, 6490.
- [9] S. Lee, G. Kwon, K. Ku, K. Yoon, S. K. Jung, H. D. Lim, K. Kang, *Adv. Mater.* **2018**, *30*, 1704682.
- [10] S. Lee, J. Hong, K. Kang, *Adv. Energy Mater.* **2020**, *10*, 2001445.
- [11] D. MacInnes, M. A. Druy, P. J. Nigrey, D. P. Nairns, A. G. MacDiarmid, A. J. Heeger, *J. Chem. Soc. – Ser. Chem. Commun.* **1981**, 317.
- [12] D. L. Williams, J. J. Byrne, J. S. Driscoll, *J. Electrochem. Soc.* **1969**, *116*, 2.
- [13] H. G. Rashev, R. B. Araujo, A. Tadjer, P. Johansson, *J. Mater. Chem. A* **2020**, *8*, 14152.
- [14] S. Tobishima, *J. Electrochem. Soc.* **1984**, *131*, 57.
- [15] S. J. Visco, L. C. DeJonghe, *J. Electrochem. Soc.* **1988**, *135*, 2905.
- [16] T. Matsunaga, T. Kubota, T. Sugimoto, M. Satoh, *Chem. Lett.* **2011**, *40*, 750.
- [17] C. Luo, O. Borodin, X. Ji, S. Hou, K. J. Gaskell, X. Fan, J. Chen, T. Deng, R. Wang, J. Jiang, C. Wang, *Proc. Natl. Acad. Sci. U.S.A.* **2018**, *115*, 2004.
- [18] C. Luo, X. Ji, S. Hou, N. Eidson, X. Fan, Y. Liang, T. Deng, J. Jiang, C. Wang, *Adv. Mater.* **2018**, *30*, 1706498.
- [19] K. Nakahara, S. Iwasa, M. Satoh, Y. Morioka, J. Iriyama, M. Suguro, E. Hasegawa, *Chem. Phys. Lett.* **2002**, *359*, 351.
- [20] Y. Morita, S. Suzuki, K. Sato, T. Takui, *Nat. Chem.* **2011**, *3*, 197.
- [21] Q. Zhao, Y. Lu, J. Chen, *Adv. Energy Mater.* **2017**, *7*, 1601792.
- [22] Y. Xu, M. Zhou, Y. Lei, *Mater. Today* **2018**, *21*, 60.
- [23] J. Y. Hwang, S. T. Myung, Y. K. Sun, *Adv. Funct. Mater.* **2018**, *28*, 1802938.
- [24] H. Kim, J. C. Kim, M. Bianchini, D. H. Seo, J. Rodriguez-Garcia, G. Ceder, *Adv. Energy Mater.* **2018**, *8*, 1702384.
- [25] D. Bin, W. Huo, Y. Yuan, J. Huang, Y. Liu, Y. Zhang, F. Dong, Y. Wang, Y. Xia, *Chem* **2020**, *6*, 968.
- [26] B. T. McAllister, L. T. Kyne, T. B. Schon, D. S. Seferos, *Joule* **2019**, *3*, 620.
- [27] D. J. Kim, D. J. Yoo, M. T. Otle, A. Prokofjevs, C. Pezzato, M. Owczarek, S. J. Lee, J. W. Choi, J. F. Stoddart, *Nat. Energy* **2019**, *4*, 51.
- [28] Y. Zhang, S. Liu, Y. Ji, J. Ma, H. Yu, *Adv. Mater.* **2018**, *30*, 1706310.
- [29] M. Armand, S. Grugeon, H. Vezin, S. Laruelle, P. Ribière, P. Poizot, J. M. Tarascon, *Nat. Mater.* **2009**, *8*, 120.
- [30] Q. Zhao, J. Wang, Y. Lu, Y. Li, G. Liang, J. Chen, *Angew. Chem., Int. Ed.* **2016**, *55*, 12528.
- [31] B. Häupler, A. Wild, U. S. Schubert, *Adv. Energy Mater.* **2015**, *5*, 1402034.
- [32] S. Wang, L. Wang, K. Zhang, Z. Zhu, Z. Tao, J. Chen, *Nano Lett.* **2013**, *13*, 4404.
- [33] N. Ogihara, T. Yasuda, Y. Kishida, T. Ohsuna, K. Miyamoto, N. Ohba, *Angew. Chem., Int. Ed.* **2014**, *53*, 11467.
- [34] G. Dai, Y. He, Z. Niu, P. He, C. Zhang, Y. Zhao, X. Zhang, H. Zhou, *Angew. Chem., Int. Ed.* **2019**, *58*, 9902.
- [35] X. Judez, L. Qiao, M. Armand, H. Zhang, *ACS Appl. Energy Mater.* **2019**, *2*, 4008.
- [36] S. Eigler, A. Hirsch, *Angew. Chem., Int. Ed.* **2014**, *53*, 7720.
- [37] D. R. Dreyer, A. D. Todd, C. W. Bielawski, *Chem. Soc. Rev.* **2014**, *43*, 5288.
- [38] D. C. Marcano, D. V. Kosynkin, J. M. Berlin, A. Sinitskii, Z. Sun, A. Slesarev, L. B. Alemany, W. Lu, J. M. Tour, *ACS Nano* **2010**, *4*, 4806.
- [39] A. Y. S. Eng, C. K. Chua, M. Pumera, *Nanoscale* **2015**, *7*, 20256.
- [40] A. Lerf, H. He, M. Forster, J. Klinowski, *J. Phys. Chem. B* **1998**, *102*, 4477.
- [41] V. Georgakilas, M. Otyepka, A. B. Bourlinos, V. Chandra, N. Kim, K. C. Kemp, P. Hobza, R. Zboril, K. S. Kim, *Chem. Rev.* **2012**, *112*, 6156.
- [42] X. Li, L. Zhi, *Chem. Soc. Rev.* **2018**, *47*, 3189.
- [43] A. Bakandritsos, M. Pykal, P. Bořski, P. Jakubec, D. D. Chronopoulos, K. Poláková, V. Georgakilas, K. Čépe, O. Tomanec, V. Ranc, A. B. Bourlinos, R. Zbořil, M. Otyepka, *ACS Nano* **2017**, *11*, 2982.
- [44] M. Blanco, D. Mosconi, M. Otyepka, M. Medved, A. Bakandritsos, S. Agnoli, G. Granozzi, *Chem. Sci.* **2019**, *10*, 9438.
- [45] Y. Heng Cheong, M. Z. M. Nasir, A. Bakandritsos, M. Pykal, P. Jakubec, R. Zbořil, M. Otyepka, M. Pumera, *ChemElectroChem* **2019**, *6*, 229.
- [46] A. Lenarda, A. Bakandritsos, M. Bevilacqua, C. Tavagnacco, M. Melchionna, A. Naldoni, T. Steklý, M. Otyepka, R. Zbořil, P. Fornasiero, *ACS Omega* **2019**, *4*, 19944.
- [47] V. Šedajová, P. Jakubec, A. Bakandritsos, V. Ranc, M. Otyepka, *Nanomaterials* **2020**, *10*, 1731.
- [48] J. Kolařík, A. Bakandritsos, Z. Bad'ura, R. Lo, G. Zoppellaro, Š. Kment, A. Naldoni, Y. Zhang, M. Petr, O. Tomanec, J. Filip, M. Otyepka, P. Hobza, R. Zbořil, *ACS Nano* **2021**, *15*, 3349.
- [49] M. Medved, G. Zoppellaro, J. Ugolotti, D. Matochová, P. Lazar, T. Pospíšil, A. Bakandritsos, J. Tuček, R. Zbořil, M. Otyepka, *Nanoscale* **2018**, *10*, 4696.

- [50] B. Pan, C.-M. Hu, L. Bai, F.-G. Zhao, L. Dong, B. Zuo, W. Zhang, X. Wang, W.-S. Li, *Adv. Funct. Mater.* **2019**, *29*, 1906076.
- [51] F.-G. Zhao, Y.-T. Kong, B. Pan, C.-M. Hu, B. Zuo, X. Dong, B. Li, W.-S. Li, *J. Mater. Chem. A* **2019**, *7*, 3353.
- [52] M. Shaibani, M. S. Mirshekarloo, R. Singh, C. D. Easton, M. C. D. Cooray, N. Eshraghi, T. Abendroth, S. Dörfler, H. Althues, S. Kaskel, A. F. Hollenkamp, M. R. Hill, M. Majumder, *Sci. Adv.* **2020**, *6*, eaay2757.
- [53] Y. Gogotsi, R. M. Penner, *ACS Nano* **2018**, *12*, 2081.
- [54] L. Fédèle, F. Sauvage, S. Gottis, C. Davoisne, E. Salager, J. N. Chotard, M. Becuwe, *Chem. Mater.* **2017**, *29*, 546.
- [55] J. Wang, H. Zhao, L. Xu, Y. Yang, G. He, Y. Du, *ACS Appl. Mater. Interfaces* **2018**, *10*, 35469.
- [56] Y. Wang, L. Lv, R. Guo, W. Huang, W. Wang, H. Chen, H. Zheng, *J. Power Sources* **2020**, *473*, 228515.
- [57] C. L. Bentley, A. M. Bond, A. F. Hollenkamp, P. J. Mahon, J. Zhang, *J. Phys. Chem. C* **2015**, *119*, 21840.
- [58] L. Fédèle, F. Sauvage, F. Lepoivre, S. Gottis, C. Davoisne, M. Courty, J.-M. M. Tarascon, M. Becuwe, *Chem. Mater.* **2019**, *31*, 6224.
- [59] E. Peled, S. Menkin, *J. Electrochem. Soc.* **2017**, *164*, A1703.
- [60] P. Verma, P. Maire, P. Novák, *Electrochim. Acta* **2010**, *55*, 6332.
- [61] H. Numazawa, K. Sato, H. Imai, Y. Oaki, *NPG Asia Mater* **2018**, *10*, 397.
- [62] Z. Sha, S. Qiu, Q. Zhang, Z. Huang, X. Cui, Y. Yang, Z. Lin, *J. Mater. Chem. A* **2019**, *7*, 23019.
- [63] L. S. Jiao, T. Wu, H. Y. Li, F. Li, L. Niu, *Chem. Commun.* **2015**, *51*, 15979.
- [64] Y. Wang, Y. Deng, Q. Qu, X. Zheng, J. Zhang, G. Liu, V. S. Battaglia, H. Zheng, *ACS Energy Lett.* **2017**, *2*, 2140.
- [65] Y. Wang, X. Zheng, Q. Qu, G. Liu, V. S. Battaglia, H. Zheng, *Carbon* **2018**, *132*, 420.
- [66] Z. Hu, S. Sayed, T. Jiang, X. Zhu, C. Lu, G. Wang, J. Sun, A. Rashid, C. Yan, L. Zhang, Z. Liu, *Adv. Energy Mater.* **2018**, *8*, 1802273.
- [67] M. Forghani, S. W. Donne, *J. Electrochem. Soc.* **2018**, *165*, A664.
- [68] Y. Huang, D. Wu, A. Dianat, M. Bobeth, T. Huang, Y. Mai, F. Zhang, G. Cuniberti, X. Feng, *J. Mater. Chem. A* **2017**, *5*, 1588.
- [69] J. Zou, C. Sole, N. E. Drewett, M. Velický, L. J. Hardwick, *J. Phys. Chem. Lett.* **2016**, *7*, 4291.
- [70] W. Su, N. Kumar, A. Krayev, M. Chaigneau, *Nat. Commun.* **2018**, *9*, 2891.
- [71] H. Zhu, J. Yin, X. Zhao, C. Wang, X. Yang, *Chem. Commun.* **2015**, *51*, 14708.
- [72] T. Yasuda, N. Ogihara, *Chem. Commun.* **2014**, *50*, 11565.
- [73] G. Wang, X. Shen, J. Yao, J. Park, *Carbon* **2009**, *47*, 2049.
- [74] G. Kresse, J. Hafner, *Phys. Rev. B* **1993**, *47*, 558.
- [75] G. Kresse, J. Furthmüller, *Phys. Rev. B* **1996**, *54*, 11169.
- [76] G. Kresse, J. Furthmüller, *Comput. Mater. Sci.* **1996**, *6*, 15.
- [77] P. E. Blöchl, *Phys. Rev. B* **1994**, *50*, 17953.
- [78] G. Kresse, D. Joubert, *Phys. Rev. B* **1999**, *59*, 1758.
- [79] J. P. Perdew, K. Burke, M. Ernzerhof, *Phys. Rev. Lett.* **1996**, *77*, 3865.
- [80] S. Grimme, *J. Comput. Chem.* **2006**, *27*, 1787.